Impinging shear layer instability in over-expanded nozzle dynamics

Cosimo Tarsia Morisco, Jean-Christophe Robinet, Julien Herpe, Didier Saucereau

Impinging shear layer instability in over-expanded nozzle dynamics

C. Tarsia Morisco,[1,a)] J.-C. Robinet,[1] J. Herpe,[2] and D. Saucereau[3]

AFFILIATIONS

[1]DynFluid Lab., Arts et Métiers Institute of Technology, 151 Bd. de l'Hôpital, Paris 75013, France
[2]Centre National d'Etudes Spatiales, Direction du Transport Spatial, 52 rue Hillairet, Paris 75012, France
[3]ArianeGroup, Forêt de Vernon, Vernon 27208, France

[a)]Author to whom correspondence should be addressed: c.tarsiamorisco@gmail.com

ABSTRACT

When rocket engine nozzles operate at a high degree of over-expansion, an internal flow separation occurs with a strong unsteady shock–wave boundary layer interaction. The global dynamics results in a low-frequency mode, which is associated with the shock displacement, and a high-frequency mode, which is correlated with the shear layer–boundary layer interaction. While the mechanism responsible for the low-frequency oscillation is known, the one in charge of the high-frequency unsteadiness is not yet clear. The scope of this paper is to provide a physical explanation for this mechanism. To do that, a delayed detached eddy simulation is used to numerically reproduce the flow in the case of a sub-scale cold-gas truncated ideal contour nozzle. The obtained results are successfully compared to the experiments and confirm the presence of two non-axisymmetric wall pressure signatures at Strouhal numbers $St = fD_j/U_j \simeq 0.2$ and 0.3 with different azimuthal selections. To reveal the origin of such modes, a power spectral density analysis is performed in the separated region. The analysis shows that both modes originate from the external shear layer and behave as "twins" in the separated region. The reason is that both modes are two sides of the same impinging shear layer instability: the acoustic mode propagates with the sound velocity, while the hydrodynamic one propagates with the supersonic shear layer velocity. In this context, the resulting self-sustained dynamics may be due to an acoustic–hydrodynamic feedback loop involving the impinging shear layer instability of the external supersonic shear layer and the separated region.

I. INTRODUCTION

The rocket nozzle's design is crucial in today's launchers. In fact, the performance of a nozzle depends on its contour and on a specific operating parameter known as nozzle pressure ratio (NPR), which represents the ratio between the combustion chamber total pressure and the ambient static pressure (p_0/p_a). To achieve optimal performance throughout the flight trajectory, the nozzles are designed to prevent any shock occurrence before the exit. Unfortunately, at ground level (high ambient pressure) or during engine start up (low total pressure), they are usually over-expanded, which causes shocks inside the divergent duct. In this condition, the resulting shock wave/boundary layer interaction triggers a self-sustained mechanism involving large separated regions, supersonic shear layers, and Mach disks. Specifically, the experiments performed by Nave and Coffey[1] on full-scale and cold-flow sub-scale models of a J-2S engine revealed for the first time the existence of two unsteady separation patterns: the one with flow reattachment, called restricted shear separation (RSS), and the other without, called free shock separation (FSS). The same nozzle was observed switching from FSS to RSS regimes at a certain value of NPR. However, the appearance of one or the other regime depends on the nozzle contour. For instance, truncated ideal contour (TIC) and conical nozzles only display FSS, whereas thrust-optimized contour (TOC) and thrust-optimized parabolic (TOP) nozzles can experience both regimes. Complexity of dynamics and the scarce numerical resources at that time first led to the launch of several experimental campaigns on two-dimensional (2D) small-angled divergent diffusers[2,3] with the intent of better understanding these unsteady phenomena. In these cases, separation is induced by strong lambda-pattern shocks and exhibits complex self-sustained dynamics driven by high-frequency turbulent structures and upstream propagating shocklets as well as low-frequency shock oscillations.[4,5] With the advancement of technology, many experimental studies were conducted on supersonic or hypersonic cold sub-scale rocket nozzle flows. In this context, Torngren[6] observed that a TIC nozzle can only experience the displacement of the internal shock if there are outer pressure fluctuations and non-reattached flow separation. The key role of the outer pressure

fluctuations in sustaining low-frequency shock oscillations was confirmed by Östlund *et al.*[7] In this experiment, the flow inside the separated region is intermittent, and the wall pressure perturbation results in a combination of a low- and high-frequency part, correlated with the shock displacement and the shear layer-boundary layer interaction, respectively. By computing a power spectral density (PSD) for each azimuthal mode of the wall pressure perturbation, Baars *et al.*[8] demonstrated that the entire power spectrum was distributed over the first two Fourier modes. In particular, the zeroth mode's energy decreases in the streamwise direction, while the first mode's energy remains relatively constant. Some experiments, carried out by Jaunet *et al.*[9] on a TIC nozzle experiencing an FSS regime at different NPR values, revealed an azimuthal axisymmetric shape (i.e., zeroth mode-like) for the low-frequency mode related to the shock displacement, as well as the existence of high-frequency organized structures, which are mainly contained in the asymmetric (i.e., first mode-like) component.

Similarly, many efforts have been devoted to study this unsteady phenomenon from a numerical perspective. Chen *et al.*,[10] by means of Reynolds-averaged Navier-Stokes (RANS) calculations, numerically showed the existence of two solutions at the same NPR value for the same nozzle geometry previously investigated by Nave and Coffey:[1] one with a recirculation bubble inside the separated region at the nozzle lip and another with a large trapped vortex behind the Mach disk. Although unsteady Reynolds-averaged Navier-Stokes (URANS) methods turned out to be very efficient in capturing unsteadiness in many compressible flows such as airfoil buffetting[11–13] as well as in evaluating low-frequency oscillations in sub-scale rocket models,[14–16] they fail when wall turbulence and self-sustained oscillations get close in terms of frequencies (e.g., less than one order of magnitude). On the other hand, solving a direct numerical simulation (DNS) or a wall-resolved large eddy simulation (WRLES) for such turbulent flows (the Reynolds number ranging between 10^5 and 10^7) is difficult or even impossible with the current technology. The compromise adopted by Olson and Lele[17] was to lower the Reynolds number of their LES calculations. In this case, although the low-frequency shock oscillation detected was slightly different from experiments, the shock position and the amplitude oscillations were significantly different, because of their strong dependence on the incoming boundary layer. Two alternative solutions involving a hybrid turbulence modeling exist: the wall-modeled large eddy simulation (WMLES)[18] or the detached eddy simulation (DES), first proposed by Spalart *et al.*[19] The interest in the DES methodology, permitting a computational resource saving for the RANS-treated boundary layer resolution, has highly increased in recent years. Deck[20] and Shams *et al.*[21] highlighted the capacity of delayed detached eddy simulations (DDESs) in capturing RSS self-sustained unsteadiness in an axisymmetric TOC nozzle. Recently, Martelli *et al.*[22] and Bakulu *et al.*[23] performed a DDES calculation of an over-expanded TIC nozzle experiencing an FSS regime. Simulations, validated with experimental measurements, confirmed for a prescribed NPR the existence of a low-frequency breathing mode as well a higher frequency contribution. The azimuthal PSD analysis of the wall pressure perturbation revealed a zeroth shock oscillation mode associated with the low-frequency as well a first mode related to the higher frequencies, which is compatible with the screech correlation proposed by Tam *et al.*[24] and the findings of Jaunet *et al.*[9] A feedback-loop model, involving the turbulent shear layers, the triple point and the second Mach disk, was proposed to explain the unsteadiness related to the first azimuthal mode.

The insight that nozzle low-frequency shock oscillations were due to a standing wave produced by an upstream and a downstream propagating traveling wave[25] is now the commonly accepted theory[22,26,27] and known as *transonic resonance*. On the contrary, the nature of the high frequency unsteadiness is not yet clear, and it is often associated with the *screech*, which is an acoustic instability prevalent in underexpanded jets.[24,28,29] In general, most of the recent studies devoted to the supersonic nozzle dynamics focus either on the internal shock dynamics or the jet noise. In the first research axis, Verma *et al.*[30] and Martelli *et al.*[31] recently showed via PSD spectra that for both experiments and LES calculations the most of energy is located at the shock foot. Here, the dynamics is related to the shock wave/boundary-layer interactions, and the dynamics is characterized by intermittency and resonance tones. In the second research axis, Edgington-Mitchell *et al.*[32] and Weightman *et al.*[33] made important progress in the understanding of the jet screech, detailing the existence of multiple feedback and receptivity paths related to the dominant resonant mode of the adapted jet. Although the transonic resonance and the screech appear to be very different, one can reasonably believe in the transition from one to the other when NPR increases and the first Mach disk moves from the nozzle throat to the nozzle exit. In support of this, the correlation formula predicting the characteristic Strouhal number St for both phenomena intersects at a Mach jet number $M_j \approx 2.1$.[9] Therefore, it is in the authors' opinion that a non-canonical screech dynamics could settle when the first Mach disk occurs before the nozzle exits. At present, the unsteady dynamics at moderate values of NPR is poorly known. The only notable works on this subject are those attributed to Jaunet *et al.*[9] and Martelli *et al.*,[22] who showed the emergence of a tonal high-frequency dynamics. The mechanism at stake in this condition is poorly known and the most accepted hypothesis conjectures about the existence of a feedback loop between the Mach disks.

The objective of this paper is providing many important insights into the understanding of the tonal high-frequency dynamics in over-expanded nozzles at moderate NPRs. To do that, the physical behavior of an over-expanded TIC nozzle experiencing an FSS regime at NPR = 9 will be reproduced by means of DDES simulations. The nozzle geometry is the same as that experimentally analyzed at Pprime Institute.[9] One of the novelty of this paper is the deployment of a PSD map in the space and frequency domain, which permits the localization of the involved high-frequency modes. The second contribution concerns the explanation of the mechanism at stake via an original acoustic–hydrodynamic feedback loop.

This paper is organized as follows: The modeling equations and the numerical method adopted in this work are detailed in Sec. II. The main flow features are qualitatively described in Sec. III. A quantitative analysis in terms of statistical quantities is addressed in Sec. IV. In the same section, a comparison with the available experimental data provided by the Pprime Institute is shown. In Sec. V, a power spectral density (PSD) is computed on a long-time simulation. In Sec. VI, the mechanism related to the high-frequency modes is described. A dimensional analysis based on time average quantities indicates that such a mechanism could be a particular impinging shear layer instability, where both modes are the expression of the same perturbation which is conveyed with different velocities. To conclude, a feedback loop mechanism involving the recirculation bubble at the nozzle lip and the impinging shear layer instability of the supersonic shear layer is proposed to explain the self-sustained high-frequency dynamics.

II. COMPUTATIONAL SETUP

A. Physical model

The methodology adopted here is based on the classical Reynolds decomposition of the flow variables into a time average and a fluctuating part and solving the governing equations only for the former. The obtained RANS equations employ a time averaging for density and pressure, while the other variables undergo an additional mass-weighted averaging. This approach is commonly known to be more convenient in the case of non-constant density, such as high-Mach compressible flows in supersonic jet nozzles. The consequent system of equations consists in the *Favre–Reynolds* averaged version of the three-dimensional (3D) Navier–Stokes equations for a compressible, viscous, heat-conducting gas, written in differential form as

$$\frac{\partial \overline{\rho}}{\partial t} + \frac{\partial}{\partial x_j}\left(\overline{\rho}\widetilde{u}_j\right) = 0, \tag{1a}$$

$$\frac{\partial}{\partial t}\left(\overline{\rho}\widetilde{u}_i\right) + \frac{\partial}{\partial x_j}\left(\overline{\rho}\widetilde{u}_i\widetilde{u}_j + \overline{p}\delta_{ij} - \widetilde{\tau}_{ij}\right) = 0, \tag{1b}$$

$$\frac{\partial}{\partial t}\left(\overline{\rho}\widetilde{E}\right) + \frac{\partial}{\partial x_j}\left[\left(\overline{\rho}\widetilde{E} + \overline{p}\right)\widetilde{u}_j - \widetilde{\tau}_{ij}\widetilde{u}_j + \widetilde{q}_j\right] = 0. \tag{1c}$$

The quantities of interest are the density $\overline{\rho}$, the streamwise, wall-normal and spanwise velocity components $\widetilde{u}_i$ in the coordinate directions x_i ($i = 1, 2, 3$), the thermodynamic pressure $\overline{p}$, and the total specific energy $\widetilde{E}$. The latter is the sum of the specific internal energy $\widetilde{e}$ and the specific kinetic one as

$$\widetilde{E} = \widetilde{e} + \frac{\widetilde{u}_i\widetilde{u}_i}{2} + \underbrace{\frac{\widetilde{u_i''u_i''}}{2}}_{K}, \tag{2}$$

where K represents the turbulent kinetic energy contribution.

The total stress tensor $\widetilde{\tau}_{ij}$ is the sum of the viscous and the Reynolds stress tensor as

$$\begin{aligned}\widetilde{\tau}_{ij} = \widetilde{\tau}_{ij}^{(l)} + \widetilde{\tau}_{ij}^{(t)} &= 2\overline{\rho}\nu\left(S_{ij} - \frac{1}{3}\frac{\partial \widetilde{u}_k}{\partial x_k}\delta_{ij}\right) - \overline{\rho}\widetilde{u_i''u_j''} \\ &= 2\overline{\rho}(\nu + \nu_t)\left(S_{ij} - \frac{1}{3}\frac{\partial \widetilde{u}_k}{\partial x_k}\delta_{ij}\right) - \frac{2}{3}\overline{\rho}K\delta_{ij},\end{aligned} \tag{3}$$

where $\tau_{ij}^{(t)}$ acts either as a model or a subgrid space filter, depending on whether a RANS approach or a LES turbulence modeling is adopted, respectively. The turbulent stress tensor, under the Boussinesq hypothesis, depends on the eddy viscosity ν_t and the strain-rate tensor $\widetilde{S}_{ij} = (\partial\widetilde{u}_i/\partial x_j + \partial\widetilde{u}_j/\partial x_i)/2$. The turbulent kinetic energy K is ignored by the fact that, in one-equation turbulence models, no relationship exists for such quantity. Kinematic molecular viscosity ν depends on temperature $\widetilde{T}$ through Sutherland's law. Similarly, the total heat flux $\widetilde{q}_j$ is the sum of a molecular and a turbulent contribution as

$$\widetilde{q}_j = \widetilde{q}_j^{(l)} + \widetilde{q}_j^{(t)} = -\rho c_p\frac{\nu}{Pr}\frac{\partial \widetilde{T}}{\partial x_j} + \overline{\rho}\widetilde{u_j''h''} = -\rho c_p\left(\frac{\nu}{Pr} + \frac{\nu_t}{Pr_t}\right)\frac{\partial \widetilde{T}}{\partial x_j}, \tag{4}$$

where $h'' = c_pT''$ is the turbulent heat flux. Pr and Pr_t are the molecular and turbulent Prandtl numbers and set at 0.72 and 0.9, respectively, as usually done in the case of air. Assuming the fluid to be a calorically perfect gas, the closing relations are

$$\overline{p} = \overline{\rho}R\widetilde{T}, \quad \widetilde{e} = c_v\widetilde{T}, \tag{5}$$

where $R = \mathcal{R}/M$ is the perfect gas constant divided by the molar mass of the fluid, commonly set at $287.1\text{Jkg}^{-1}\,\text{K}^{-1}$ for air and c_v is the specific heat capacity at constant volume. The latter is linked to the specific heat capacity at constant pressure c_p by the specific heat ratio $\gamma = c_p/c_v$, set at 1.4 for diatomic gas.

B. Turbulence modeling

The turbulence formulation adopted here is made by means of a DDES,[34] based on the Spalart–Allmaras turbulence model with neglecting trip terms.[35,36] The latter consists of a simple convection–diffusion equation for the pseudo-turbulent viscosity variable $\widetilde{\nu}$ where the source term is obtained as a balance between a production term $\mathcal{P}$ and a destruction term $\mathcal{D}$ associated with the same quantity, as

$$\begin{aligned}&\frac{\partial(\overline{\rho}\widetilde{\nu})}{\partial t} + \frac{\partial\left(\overline{\rho}\widetilde{\nu}u_j\right)}{\partial x_j} - \frac{1}{\sigma}\frac{\partial}{\partial x_j}\left[\left(\overline{\rho}\nu + \overline{\rho}\widetilde{\nu}\right)\frac{\partial \widetilde{\nu}}{\partial x_j}\right] \\ &\quad = \underbrace{c_{b1}\widetilde{S}\overline{\rho}\widetilde{\nu} + \frac{c_{b2}}{\sigma}\frac{\partial \widetilde{\nu}}{\partial x_j}\frac{\partial \overline{\rho}\widetilde{\nu}}{\partial x_j}}_{\mathcal{P}} \underbrace{-\overline{\rho}c_{w1}f_w\left(\frac{\widetilde{\nu}}{d_w}\right)^2}_{\mathcal{D}}.\end{aligned} \tag{6}$$

The presence of density $\overline{\rho}$ in the above formula is justified by the will of extending the above equation to compressible flows.[37] c_{b1}, c_{b2}, σ, and c_{w1} are standard-defined constants, while $\widetilde{S}$ and f_w are a modified vorticity and a near-wall function, respectively. In addition, the *Edwards modification*[38] is used to improve the robustness and the near-wall numerical behavior of the model.

In the DDES framework, the destruction term $\mathcal{D}$ is made grid-sensitive by replacing the near-wall distance d_w with $\widetilde{d}$ as

$$\begin{aligned}f_d &= 1 - \tanh\left(\left(C_1r_d\right)^3\right), \quad r_d = \frac{\widetilde{\nu}}{\sqrt{\frac{\partial u_i}{\partial x_j}\frac{\partial u_i}{\partial x_j}\kappa^2d_w^2}}, \\ \widetilde{d} &= d_w - f_d\cdot\max(0, d_w - \Psi C_{DES}\Delta),\end{aligned} \tag{7}$$

where f_d is the boundary layer shielding function, which is supposed to be 0 in the RANS region and 1 in the LES one. κ is the von Kármán constant, Δ is the subgrid filter width, and Ψ is the function designed to prevent the erroneous activation of the turbulence model near-wall functions in low viscosity LES regions.[34] In this work, the adjusted version derived by Mockett[39] for the Edwards modification is used. Finally, C_1 and C_{DES} are two calibrated coefficients set at 16 and 0.2, respectively, as by Martelli *et al.*[22]

According to Deck,[40] though f_d was conceived to avoid any LES incursion inside the attached boundary layer, an exclusive use of $\Delta = \Delta_{\max} = \max(\Delta x_i)$ as subgrid scale would delay the formation of instabilities in free shear layers. For this reason, here the modified version of the Extended Delayed Detached Eddy Simulation (EDDES)[41,42] proposed by Pont[43] is employed as

$$\Delta = \begin{cases}\Delta_{\max}, & f_d < f_{d0}, \\ \Delta_\omega, & f_d \geq f_{d0},\end{cases} \quad \Delta_\omega = \sqrt{\frac{\sum_{i=1}^{N_f}\boldsymbol{\omega}\cdot\mathbf{S}_i}{2||\boldsymbol{\omega}||}}, \tag{8}$$

where $\mathbf{S}$ and $\boldsymbol{\omega}$ are the vector of the cell face projections in the coordinate directions x_i and the local vorticity, respectively. f_{d0} is the shielding function threshold value for the switching between the two criteria and set at 0.8 as usual in the literature.

C. Flow solver description

The code used for all simulations here shown is `Phoenix`,[44] an in-house finite-volume structured code performing RANS/URANS and DDES calculations, developed at *Pprime Institute* in collaboration with *Dynfluid Laboratory*. In the present work, the dimensionless compressible RANS equations corresponding to Eqs. (1a)–(1c) are solved, after being re-arranged in the following conservative form:

$$\frac{\partial}{\partial t}\int_{\Omega}\mathbf{q}\ d\Omega + \underbrace{\oint_{\partial\Omega}(\mathbf{F}_c - \mathbf{F}_v)\mathbf{n}\ dS}_{\mathbf{R}(\mathbf{q})} = \mathbf{0}, \tag{9}$$

with $\mathbf{q} = [\rho, \mathbf{m}, \rho E]^T$ and $\mathrm{m}_i = \rho u_i$. $\mathbf{R}(\mathbf{q})$ is the residual vector composed of $\mathbf{F_c}$ and $\mathbf{F}_v$, the convective and viscous flux vector, respectively. Any needed gradient is computed by means of *Green's theorem* using a second-order accurate finite difference formula for the face value quantities. The residual vector is discretized by a third-order directional noncompact (DNC) scheme with the scalar dissipation scheme of Jameson, Schmidt, and Turkel (JST).[45] The one-equation turbulence model in Eq. (6) is rearranged similarly as Eq. (9) and discretized with a second-order TVD scheme[46] with *Harten's* entropy correction.

An implicit loosely coupled algorithm is used to integrate the RANS equations and the turbulence equation separately.[47,48] Particularly, a dual-time stepping (DTS) Technique is used to march in time in concert with a matrix-free method,[49,50] which provides a fast and low-storage convergence for the inner fictitious steady problem. A constant Courant–Friedrichs–Lewy (CFL) number is used.

D. Numerical strategy

The nozzle geometry considered in this work is a truncated ideal contour (TIC), obtained by means of a two-dimensional axisymmetric method of characteristics (MOC) technique with a boundary layer correction based on Delery's strategies.[51] The resulting nozzle shape is provided in Fig. 1. The geometrical properties are listed in Table I and expressed with respect to the throat radius R_t.

The reference quantities chosen are the free-stream stagnation ones ($a_{0,\infty}$, $\rho_{0,\infty}$, $T_{0,\infty}$). Under the assumption of isentropically resting flow at free-stream conditions, $T_{0,\infty}$ and $p_{0,\infty}$ are set equal to the nozzle combustion chamber temperature (260 K) and the standard sea-level pressure (0.1 MPa), respectively. The reference length considered

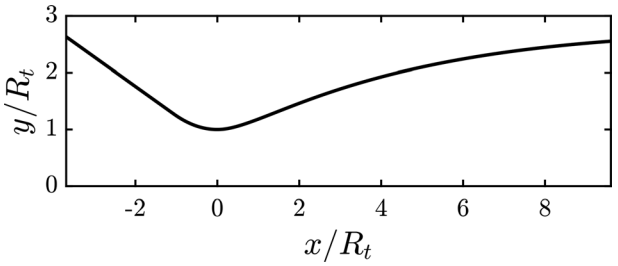

FIG. 1. TIC nozzle axisymmetric geometry, $M_d = 3.5$.

TABLE I. TIC nozzle shape parameters.

Design Mach	$M_d = 3.5$
Throat radius	R_t
Exit radius	$R_e/R_t = 2.55$
Divergent length	$L/R_t = 9.63$
Convergent length	$l/R_t = 3.68$
Curvature radius	$\rho = R_c/R_t = 10$

is the nozzle throat radius, i.e., $L_{\mathrm{ref}} = R_t$. The value of the throat radius R_t is a confidential information.

The Reynolds number, based on the free-stream stagnation quantities, is consequently

$$Re_0^{\infty} = \frac{\rho_{0,\infty} a_{0,\infty} L_{\mathrm{ref}}}{\mu_{0,\infty}} = 5.0 \times 10^5. \tag{10}$$

The three-dimensional computational domain includes the nozzle and the far-field region, and it is discretized with nine blocks. The nozzle and the external region obtained from its extrusion up to the outlet are made up of five blocks meshed together with an O–H topology to prevent any singularity about the longitudinal axis (see Fig. 2). The grid was generated with the Cadence Fidelity Pointwise software.

The far-field region is composed of additional 4 O-grid blocks. Domain boundaries are four and two times the overall nozzle length ($L^* = l + L$) far from the nozzle exit in the streamwise and radial directions, respectively. The resulting multiblock mesh is shown in Fig. 3. For the O–H structured blocks of the domain, the grid resolution is $n_x = 813$ in the longitudinal direction (697 of which within the nozzle and 117 in the exterior part) and $n_r = 177$ ($n_\theta = 89$) in the radial (azimuthal) direction for each of the four blocks surrounding the core nozzle. The longitudinal cut plane of the grid is shown in Fig. 4, showing the grid refinement in the nozzle core. The 4O-grid blocks in the exterior part have 117, 309, and 352 points in the longitudinal (x), radial (r), and azimuthal (θ) directions, respectively. The discretization was driven by the will of ensuring as much as possible

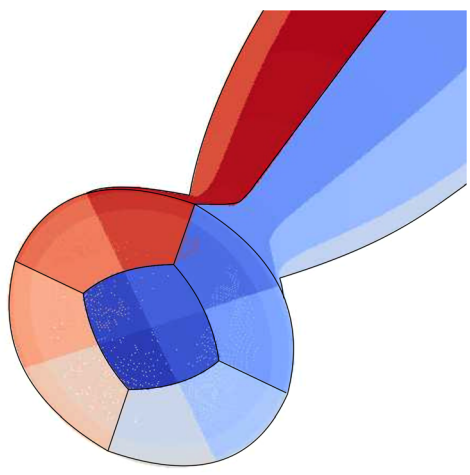

FIG. 2. Visualization of the O–H topology grid structure.

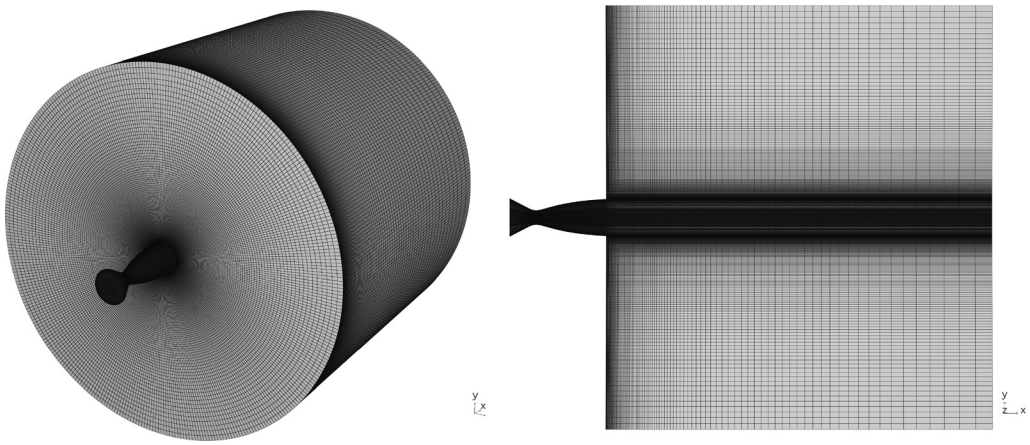

FIG. 3. Computational grid used in the calculation. Axonometric view (left) and longitudinal cut plane (right). The nozzle length is L^*. Domain boundaries are $4 \times L^*$ and $2 \times L^*$ far from the nozzle exit in the streamwise and radial directions, respectively.

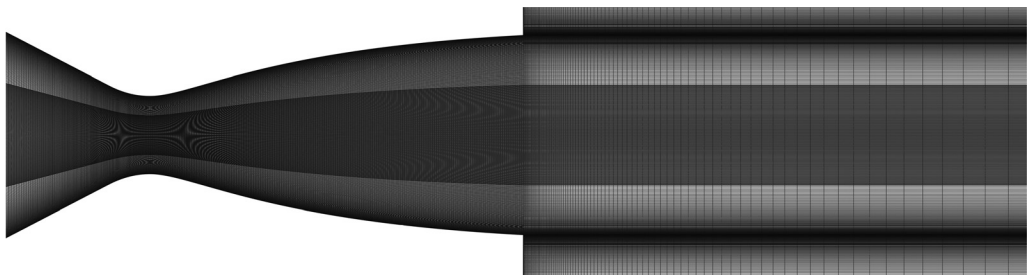

FIG. 4. Computational grid used in the calculation. Longitudinal cut plane.

quasi-isotropic cells in the streamwise and tangential directions inside the nozzle. The resulting grid consists in 69×10^6 hexahedra.

Given that the objective of this work is the analysis of the mechanism related to the tonal components of the self-sustained unsteadiness (i.e., $St = 0.2$ and $St = 0.3$), all the temporal quantities will be expressed in terms of the period of such dimensionless frequencies. In this regard, the physical time step considered is 200 times smaller than the period of a single-frequency wave oscillating at $St = 0.2$ (see Table II). The grid resolution is based on a previous convergence study on the separation point provided by a steady RANS calculation, used to initialize the corresponding DDES calculation. It is worth pointing out that no specific inflow boundary condition is used to promote the development of resolved turbulence. Turbulent structures naturally developed near the nozzle exit and propagate throughout the domain during a long numerical transient t_0, as one can see from the Table II. After that, a self-sustained unsteadiness settles without any need to be sown. The maximum value of y^+ is about 12; therefore, a wall function boundary condition with adiabatic temperature and pressure extrapolation is prescribed at the nozzle walls. The nozzle inflow is assumed to be subsonic, and the primitive variables $(\rho, p, \mathbf{u})$ are computed here by coupling the linearized outgoing characteristic equation, the 1D isentropic relations, and the state equation by imposing the total temperature $T_0 = T_{0,\infty}$, total pressure $p_0 = \mathrm{NPR} p_a$, and the flow angle $\alpha = 0°$.[52,53] The resulting system of equations is iteratively solved by a Newton method. The outflow is assumed to be subsonic with a prescribed pressure $p_a = p_{0,\infty}$, while both the far-field lateral boundaries and the fictitious wall at the nozzle exit are treated with a non-reflective boundary condition[54] and imposed free-stream Mach number $M_\infty = 0.05$.

The numerical parameters used for DDES calculations are listed in Table II.

TABLE II. Numerical parameters.

Physical time step	$\Delta t = T_{St=0.2}/200$
Numerical transient time	$t_0 = 24\ T_{St=0.2}$
DTS iterations CFL	30
DTS iterations	60
JST k_2 coefficient	0.5
JST k_4 coefficient	0.09
Harten coefficient	0.05

III. FLOWFIELD FEATURES

Before analyzing the flow from a statistical point of view, it would be interesting to take a look to its instantaneous features. Let us consider the traceless part of the gradient velocity tensor $A = \nabla \mathbf{u} - \frac{1}{3} \nabla \cdot \mathbf{u}$. The Q-criterion is here defined as the second invariant of the tensor A.[22] Positive values of Q correspond to regions in the flowfield where

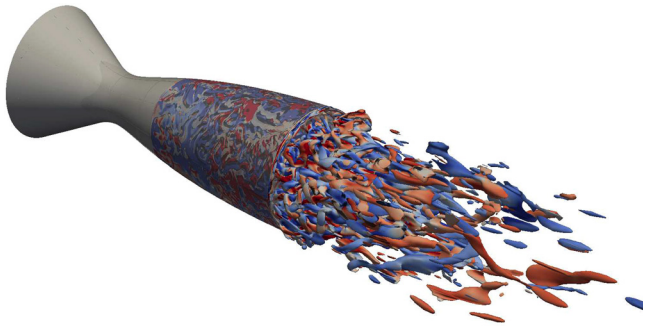

FIG. 5. Q-criterion colored by the streamwise velocity component.

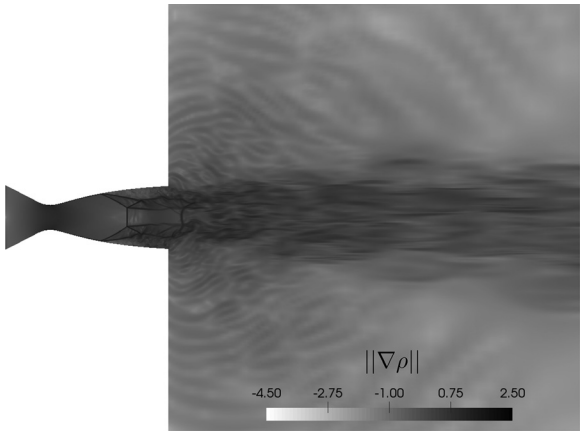

FIG. 6. Unsteady DDES solution at NPR = 9. Contours of density gradient ($|\nabla\rho|$) on a longitudinal view. Logarithmic scale.

vorticity dominates strain. The iso-surface of Q, colored by the streamwise velocity component, is shown in Fig. 5. In this DDES simulation, the reader can note that the unsteadiness triggering is located near the wall separation point. The shape of the flow structures is more and more anisotropic and elongated in the advection direction, downstream.

To enrich this preliminary and qualitative analysis, a longitudinal view of the instantaneous density gradient norm $\| \nabla\rho \|$ is provided in Fig. 6. At the pressure ratio considered in this work, i.e., NPR = 9, the nozzle does not operate in adapted conditions. In this regard, by means of a 2D MOC, it is possible to show that adaptation is obtained at NPR $\simeq$ 18.[55] On the other hand, in the case here considered, the flow recompresses inside the nozzle by oblique shock waves. Being the angle of these oblique shock waves greater than the critical one compatible with a regular reflection, a Mach reflection settles. Two Mach disks are clearly visible. The first one is inside the divergent part of the nozzle, while the second one just downstream of the nozzle exit. As shown in Fig. 6, the over-expansion of the nozzle leads to a massive separation of the turbulent boundary layer in the form of a free shock separation (FSS). In these conditions, a supersonic jet remains confined by two shear layers: the first one coming from the separation point (which will be called external shear layer hereafter) and the second one coming from the triple point (denoted as internal shear layer). Figure 7 shows a closer view of this zone. Clearly, the most of the unsteady dynamics is located both in the separated zone and inside the supersonic jet. Particularly, it seems that such unsteadiness, transmitted by the shear layers, leads to significant oscillations (in amplitude) of the second Mach disk. The reason for that seems to be some instabilities originating close the separation point. Here, some compression waves similar to shocklets (already observed in Ref. 10) radiate from the internal shear layer to the external one. These structures grow when advecting in the streamwise direction and eventually are triggered where the reflected shock coming from the triple point hits the external shear layer. The same phenomenon was observed by Martelli *et al.*[22] From this point to downstream, more and more turbulent eddies seem to detach and propagate upstream, possibly closing the loop. Moreover, those structures detaching from the external shear layer near the second Mach disk seem to interact with the nozzle lip, from which some aero-acoustic radiation appears to emanate into the external environment. The fully three-dimensional aspect of the flow is well visible in the asymmetric dynamics of the shear layers. A transverse view of the second Mach disk is given in Fig. 7, on the right. A pretty complex dynamics in the azimuthal direction is well visible and will be analyzed in Sec. V. It is important to note that the first Mach disk is also unsteady but it oscillates with a lower amplitude. After qualitatively detailing the instantaneous features of the flow, in Sec. IV, we will analyze its statistics and compare them with the experimental results provided by the Pprime Institute.[9]

IV. STATISTICAL ANALYSIS

The time average wall pressure $\overline{p_w}$ along the streamwise direction is shown in Fig. 8. Blue, red, and black lines correspond to DDES simulations performed on the same TIC nozzle for NPR = [6, 9, 12],

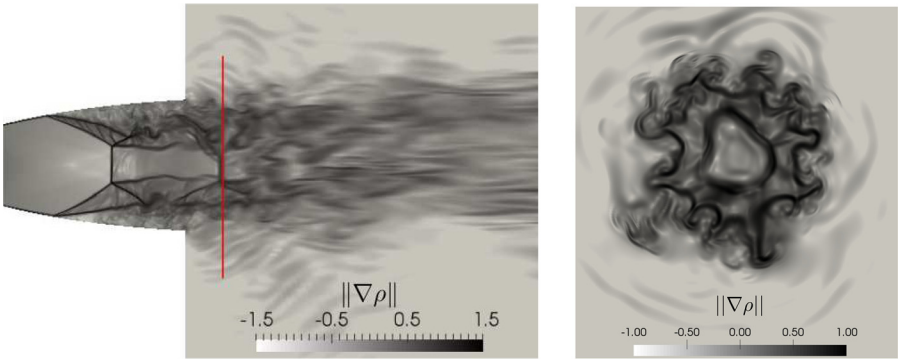

FIG. 7. Contours of the density gradient (logarithmic scale). Longitudinal view (left) and transverse view (right) at $x/L = 1.142$. The red line indicates the transverse plane.

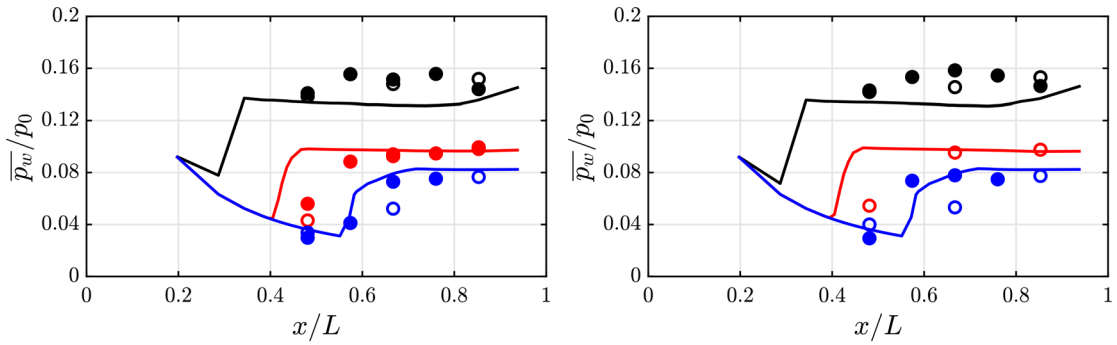

FIG. 8. Comparison between experiments and DDES in terms of mean wall pressure along the same generatrix for different NPRs. Solid lines, DDES; filled (respectively, empty) circles, measurements from experimental campaign of 2016 (respectively, 2019). Black, red, and blue color stands for NPR = [6, 9, 12] data, respectively.

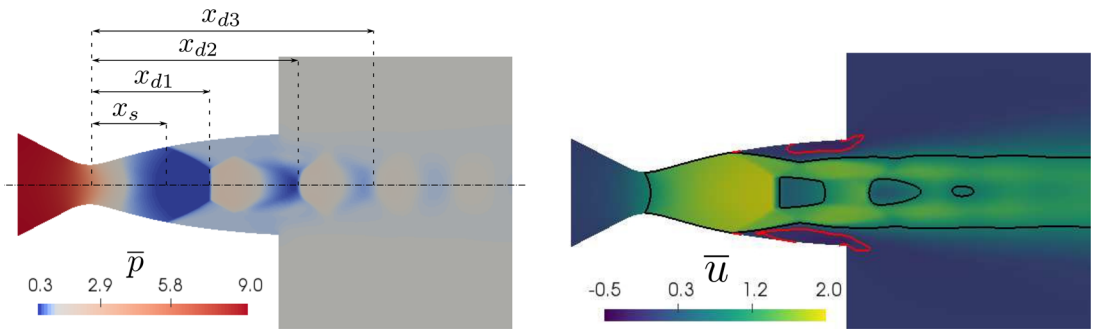

FIG. 9. Mean DDES solution at NPR = 9, longitudinal view. On the left, contours of the mean pressure ratio $\overline{p} = \overline{P}/p_a$, where P (Pa) is the dimensional pressure. The gray color in the color-map corresponds to $\overline{p} = \overline{P}/p_a = 1$ (i.e., where mean pressure $\overline{P}$ matches ambient pressure p_a) to highlight the shock system. x_s is the average separation point, while $x_d = (x_{d1}, x_{d2}, x_{d3})$ the average location of the first, second, and third Mach Disk. On the right, contours of dimensionless streamwise velocity $\overline{u} = \overline{U}/a_{0,\infty}$. The continuous black and red lines are the sonic line and 0-value streamwise velocity isolines, respectively.

respectively. Numerical results concerning NPR = 6 and NPR = 12 will not be detailed here. If the reader is interested can refer to Ref. 55. In this figure, the over-expanded state of the TIC nozzle under consideration is well visible. The wall pressure $\overline{p_w}$ isentropically decreases in the streamwise direction down to separation. Here, an oblique shock occurs and pressure immediately jumps up to a plateau value reaching ambient pressure at the exit. This almost constant trend for the wall pressure proves that flow does not reattach as in the case of nozzles experiencing an FSS regime. DDES calculations are here compared with two experimental campaigns carried out on the same nozzle at the same operating conditions. The data related to these two campaigns are indicated with filled and empty circles. In view of the uncertainty in measurements, the pressure trend is in a good approximation with experiments given that numerical data fall almost between the experimental ones coming from both campaigns. Only a slight discrepancy is observed in separation point capturing. It is in the author's opinion that the separation point upstream shifting is due to a non-perfect RANS/LES transition, as already mentioned in Ref. 22. The data in Figs. 8(a) and 8(b) are extracted from two generatrix at the azimuthal positions $\theta = 0°$ and $\theta = 180°$ in the counterclockwise rotation, respectively. The position $\theta = 0°$ (respectively, $\theta = 180°$) corresponds to the positive (respectively, negative) wall-normal y coordinate. The mutual coherence in the numerical results corresponding to these different azimuthal positions confirms the mean flow axisymmetricity.

The time average DDES solution at NPR = 9 is shown in Fig. 9, in terms of pressure field $\overline{p}$ (a) and streamwise velocity field $\overline{u}$ (b). As expected, the resulting shock system is composed of a first Mach disk (located at x_{d1}), originating from the oblique shock coming from the separation point, and a series of expansion fans and compression waves forming a cellular pattern of Mach disks in the streamwise direction. Only two Mach disks (located at x_{d2} and x_{d3}) are visible in this periodic spatial structure, while the others are necessarily smoothed by the grid decreasing refinement toward the outlet of the domain. As it happens for over-expanded nozzle flows, the separation point (x_s) is inside the nozzle. The coordinates of such points in the streamwise direction are listed in Table III. Black lines in Fig. 9(b) are sonic lines,

TABLE III. Time average (mean) DDES solution at NPR = 9. Location in the streamwise direction x of: separation point x_s, first Mach disk x_{d1}, second Mach disk x_{d2}, and third Mach disk x_{d3}.

x_s/L	x_{d1}/L	x_{d2}/L	x_{d3}/L
0.426	0.669	1.116	1.526

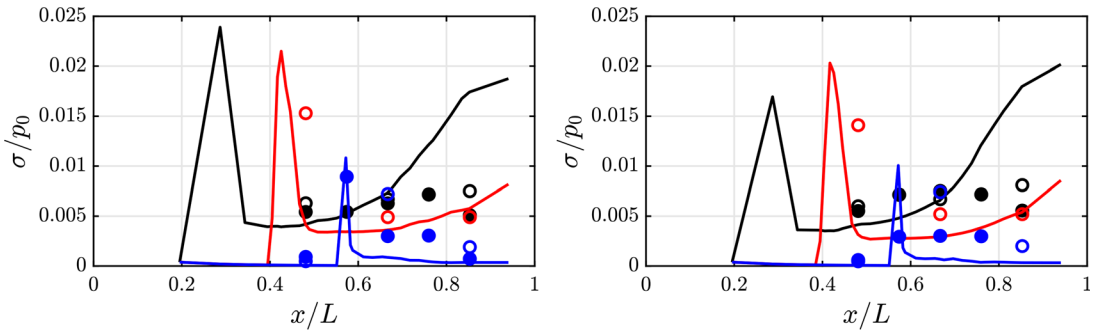

FIG. 10. Comparison between experiments and DDES in terms of wall pressure RMS along the same generatrix for different NPRs. Solid lines, DDES; filled (respectively, empty) circles, measurements from experimental campaign of 2016 (respectively, 2019). Black, red, and blue color stands for NPR = [6, 9, 12] data, respectively.

which permit identifying two annular regions: the inner one limited by the internal shear layer, and the second one between the internal and the external shear layer. Particularly, the latter appears to be strictly supersonic while the former is subsonic just downstream a Mach disk and accelerates up to supersonic conditions just before the following Mach disk. This is possible thanks to the external annular region that, "bending" toward the internal one because of the expansion fans, reduces the inner region flow section. The red lines are null-streamwise velocity isolines, which denote the presence of some recirculation at the nozzle lip. This feature is a key aspect for the explanation of the dynamics inside the separated region in Sec. VI. As one can state by observing this figure with special attention, the mean flow seems to be not perfectly axisymmetric: this happens because, as we will see in Sec. V, the unsteady solution is very rich in terms of frequency spectrum with a large amount of energy located at very low frequency. Consequently, since a mean flow is statistically converged only when all its frequency content is converged, the higher is the energy present at low frequencies, the higher is the time necessary to converge this solution. For this reason, in the case of highly unsteady flows, the time required is so huge that it is even not affordable in terms of computational resources. It should be remembered that the scope of this paper is providing a physical explanation to the mechanism related to the high frequency spikes at $St = 0.2$ and $St = 0.3$. Thus, as a trade-off between spectral content convergence and computational cost, the signal length over which the unsteady solution was averaged is 100 periods of a single-frequency wave oscillating at $St = 0.2$. From a quantitative point of view, such simulation provides the resolvability of about $\Delta_{St} = 0.002$, which guarantees a good statistical convergence for the high frequency part of the spectrum. It is worth noting that the restitution time for a 1.5-periods simulation corresponds to 24 h on 308 processors of the national HPC facilities (i.e., Occigen). Accordingly, the total computational cost amounts to 4×10^6 h.

Concerning the deviations from the time average solution, Fig. 10 gives interesting insights. Standard deviation (σ), i.e., the RMS of the unsteady solution, shows a sharp spike at the separation point due to shock oscillations, as shown in previous works about nozzles experiencing an FSS regime.[7,22] The pressure signal at the streamwise location of this spike is shown in Fig. 11. As one can state by observing this figure, pressure jumps between two levels, one corresponding to a point outside the separated region and the other inside. This is the result of an intermittency inside the separated region, already observed early by Kistler[56] for supersonic flows over a forward-facing step and later by Östlund *et al.*[7] in nozzle flows experiencing an FSS regime.

V. SPECTRAL ANALYSIS

The analysis of the unsteady wall pressure perturbation p' is performed by means of a power spectral density (PSD), referred here with $\langle p_m p_m^* \rangle$, where p_m is its azimuthal decomposition defined as

$$p_m(x,t) = \frac{1}{2\pi}\int_0^{2\pi} p'(x,\theta,t)\mathrm{e}^{im\theta}\, d\theta \quad \text{with} \quad m = 0, 1, 2\ , \ldots,\ n.$$

Frequency is expressed in terms of the Strouhal number ($St = fD_j/U_j$), which is based on the fully expanded jet velocity (U_j) and the fully expanded jet diameter (D_j), given by

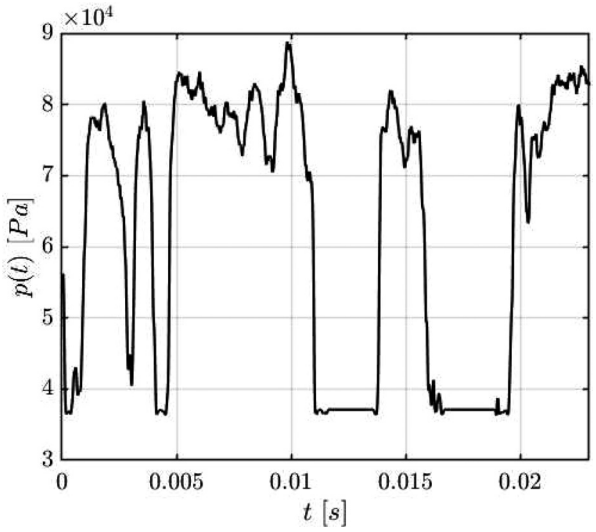

FIG. 11. Unsteady DDES solution at NPR = 9. Wall pressure signal at the separation point x_s/L.

$$U_j = \sqrt{\gamma R T_0}\,\frac{M_j}{\sqrt{1+\dfrac{\gamma-1}{2}M_j^2}},$$
$$D_j = D_e\left(\frac{M_d}{M_j}\right)^{0.5}\left(\frac{1+\dfrac{\gamma-1}{2}M_j^2}{1+\dfrac{\gamma-1}{2}M_d^2}\right)^{\frac{\gamma+1}{4(\gamma-1)}}, \tag{11}$$

where T_0 is the stagnation temperature, D_e is the nozzle exit diameter, and M_j is the fully expanded jet Mach number defined as

$$M_j = \left[\left(\mathrm{NPR}^{(\gamma-1)/\gamma}-1\right)\frac{2}{(\gamma-1)}\right]^{1/2}. \tag{12}$$

The PSDs are computed using Welch's method,[57] i.e., subdividing the pressure signal into N blocks with 50% overlap that are then individually Fourier-transformed. The PSD spectrum is finally obtained by averaging the discrete Fourier transform (DFT) energy spectra of the various segments, in order to minimize the variance of the power spectral density estimator. To better recognize the dominant frequency ranges, PSDs are here shown in a pre-multiplied form and normalized by the dynamic pressure of the fully expanded jet $\gamma P_j M_j^2$ (i.e., $St^*\langle p_m p_m^*\rangle/\gamma P_j M_j^2$). P_j is the ambient pressure p_a.

By means of PSD, the unsteady wall pressure perturbation has revealed specific signatures in frequency. First Baars *et al.*,[8] and later Jaunet *et al.*[9] for the same TIC nozzle considered here, shown a precise azimuthal selection for the spikes present in the PSD spectrum. For this reason, a PSD of the first three wall pressure perturbation azimuthal modes at $x/L = 0.665$ is presented in Fig. 12. For the case at NPR = 9, the DDES reproduces the same distribution provided by the experiments in terms of azimuthal selection for each frequency component. Particularly, the component at $St = 0.3$ is associated almost exclusively with the mode $m = 2$, while the more energetic $St = 0.2$ component is related to the mode $m = 1$. The high-frequency bump ($St \approx 1$) contributes in terms of energy to all azimuthal modes, confirming to be related to stochastic turbulent structures. In contrast to the experiments, the most energetic contribution in the DDES calculation is due to the mode $m = 0$, which is related to a low-frequency bump at $St \approx 0.02$. It should be remembered that, even though the cutoff frequency of the sensors is around 40 kHz (Ref. 9) and it is compatible with the frequency sampling of the recorded fields [$1/(10 \times \Delta t) \approx 42.5$ kHz], the total simulation time ($T \approx 0.05$ s) is not equivalent to the experimental signal length ($T \approx 90$ s). From a qualitative point of view, the spikes at $St = 0.2$ and $St = 0.3$, as well as the high-frequency bump at $1 < St < 2$, were not observed changing anymore in terms of frequency starting from a 60-period recording. However, in order to have a better convergence in terms of amplitude for such portion of the spectrum, a longer signal (i.e., 100-period one) was recorded. As mentioned in Sec. IV, such longer recording guarantees an error estimate of about $\Delta_{St} = 0.002$. This means that frequencies below Δ_{St} are not captured. However, there is no guarantee that higher frequencies are statistically converged. In fact, if 60 periods are required for the emergence of the spikes at $St = 0.2$ and $St = 0.3$, it appears reasonable that a low-frequency broad band could need even more periods to be statistically converged. In fact, the authors observed that the energy of the bump at $St \approx 0.02$ decreases with increasing signal length. In this simulation, this frequency is discretized "only" with ten periods. Therefore, it is in the authors' opinion that, with enough computational resources, the numerical spectra could resemble more to the experimental one.

In order to investigate the nature of the different modal contributions, the azimuthal PSD of wall pressure perturbations was computed for several axial positions. The resulting map is shown in Fig. 13. The low-frequency energy ($St < 0.1$) as well the high-frequency one appears to be similarly distributed in all three azimuthal components. The resulting low-frequency component, located around the average separation point ($\overline{x}/L \approx 0.45$), is compatible with the stochastic behavior characterizing a shock-wave boundary layer interactions and confirms what observed in Jaunet *et al.*[9] On the other hand, the high frequency contribution located near the nozzle lip are related to the fully turbulent structures of a recirculation bubble. As previously shown in similar cases,[8,9,22] the zeroth azimuthal PSD component

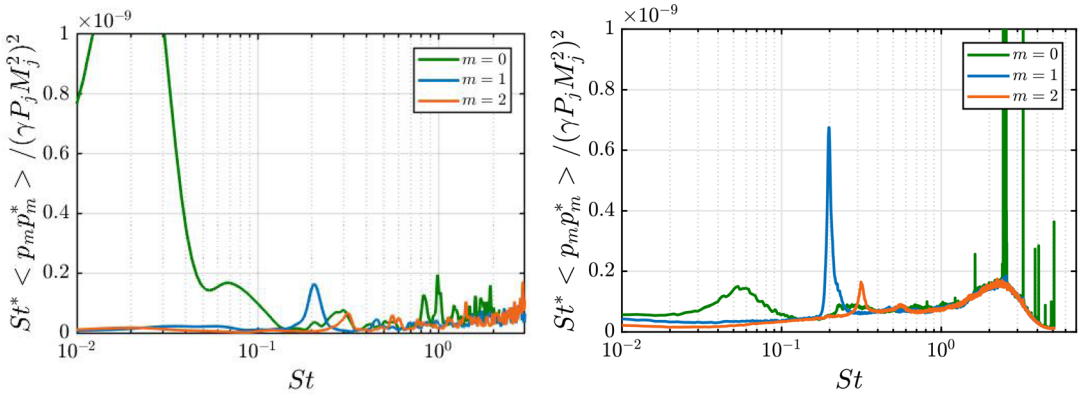

FIG. 12. Pre-multiplied PSD Main of wall pressure perturbation main azimuthal modes at a fixed streamwise location. Green, light-blue, and orange color stand for mode $m = 0$, 1, 2, respectively.

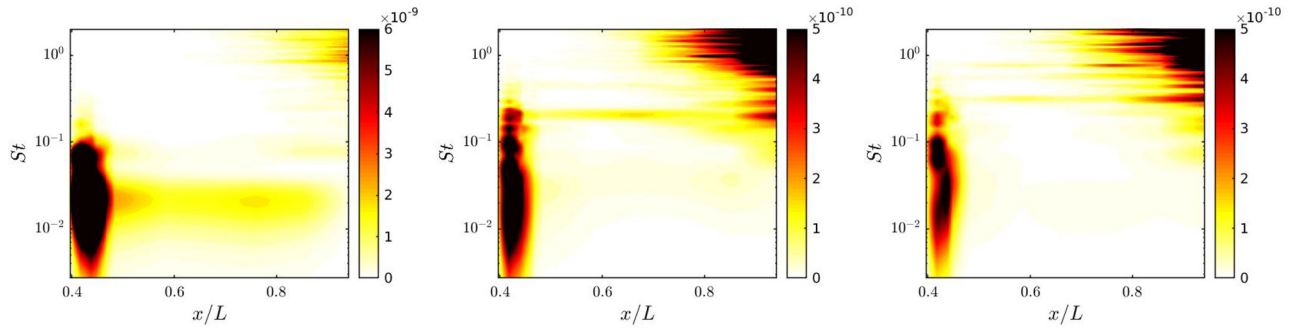

FIG. 13. Contours of the main azimuthal mode of the wall pressure perturbation pre-multiplied PSD in the space and frequency domain.

dominates the energy wave-number spectrum and decreases in the axial direction toward the nozzle exit. Moreover, two specific high-frequency wall pressure signatures at $St = 0.2$ and $St = 0.3$ are well visible in the spectrum and related to the first and second azimuthal mode, respectively. Particularly, these two spikes seem to emerge over the entire spectrum in the separated region sufficiently far from both the separation point and the nozzle lip at around $0.5 < x/L < 0.7$.

Although the wall pressure perturbation PSD indicates the region where these signatures in the frequency domain are prevalent, it gives no information about the growth area of the structures related to them. For this reason, an accurate investigation in the spatial domain inside the nozzle was conducted by using several pressure probes located (i) in the region between the external shear layer and the wall, (ii) on the nozzle axis. The positions of the probes put on the shear layers, on the axis and at the wall are shown in Fig. 14. We did not purposely indicate all the probes placed in the separated region in order not to undermine the sketch clarity. The time signal recorded throughout the DDES simulation permitted to provide a 3D map in terms of pressure perturbation azimuthal PSD.

A. Spatial organization of the pressure frequency content

To better understand the nature of the different frequency content contributions, the main azimuthal modes PSD was computed at different axial and radial locations. Figure 15 shows the spatial distribution of the zeroth azimuthal mode inside the nozzle. As one can state by observing this figure, near the average separation point ($x/L \approx 0.5$), the structures characterized by this modal contribution seem to have birth in the external shear layer with only those at

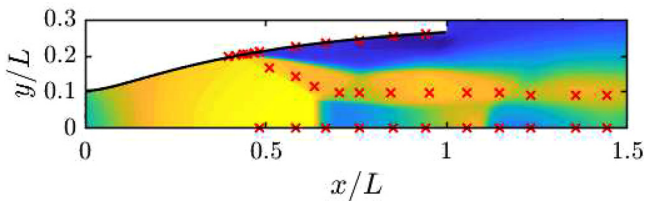

FIG. 14. Time average streamwise velocity field at NPR = 9. Probes' locations for the azimuthal PSD 3D map are denoted with red crosses. L is the divergent length.

Strouhal number $St \approx 0.02$ propagating toward the separated region. Moving from the separation point downstream, this selection is more and more evident until approaching the triple point ($x/L \approx 0.7$), where the external shear layer shows a broadband high energy content ($St < 0.2$), a signature at $St = 0.3$ and fully developed turbulent structures at high frequencies ($St \approx 1$) detaching from the shear layer and rapidly dissipating in the separated region. Moving more downstream up to the nozzle lip, it seems that the region near the shear layer becomes less and less energetic in favor of the turbulent structures which manage to "survive" in the separated region.

Now, let us analyze the first azimuthal modal frequency contribution. In Fig. 16, the reader can note that near the separation point the spectral content exhibits a low frequency bump around $St \approx 0.02$ as well as the emergence of an energetic spike at $St \approx 0.1$ with its subharmonics at $St \approx 0.2$ and $St \approx 0.3$. At this point, it seems that there are no structures departing in the separated region, but if we focus our attention near the wall [see Fig. 13(b)], where the hydrodynamics energetic content in the shear layer is no more present, we can capture the presence of a high-frequency signature at $St \approx 0.2$. This probably indicates that only those structures at this particular frequency detach and depart in the separated region. Moving downstream along the external shear layer at $x/L \approx 0.58$, the previous observation becomes the prevalent scenario. The low-frequency energy contribution seems to lower in favor of a more and more energetic signature at $St \approx 0.2$ and suggesting an energy transfer from the shear layer to some high frequency structures which spread in the separated region. At this axial location, we can see an energy spike at the level of the external shear layer, which decreases in the radial direction. However, this scenario changes while approaching the average first Mach disk position ($x/L \approx 0.63$). Here, the signature at $St = 0.2$ seems to get another "burst of energy" at $y/L \approx 0.15$. This "extra" energy contribution does not dissipate quick as before, and the signature at $St = 0.2$ seems to stay energetic throughout the separated region up to the wall. The same conditions still exists at least at $x/L = 0.7$ where, in the vicinity of the triple point, the external shear layer becomes immediately more energetic as well as the structures related to the signature at $St \approx 0.2$. If we take a look at Fig. 13(b), it is possible to see for this mode an energy boost even at the wall at $0.63 < x/L < 0.7$. Moreover, even though the external shear layer is even more energetic at $x/L = 0.76$, the energy of the signature at $St = 0.2$ decreases faster in the radial direction as happens before $x/L \approx 0.58$. Moving more and more downstream, this mode is

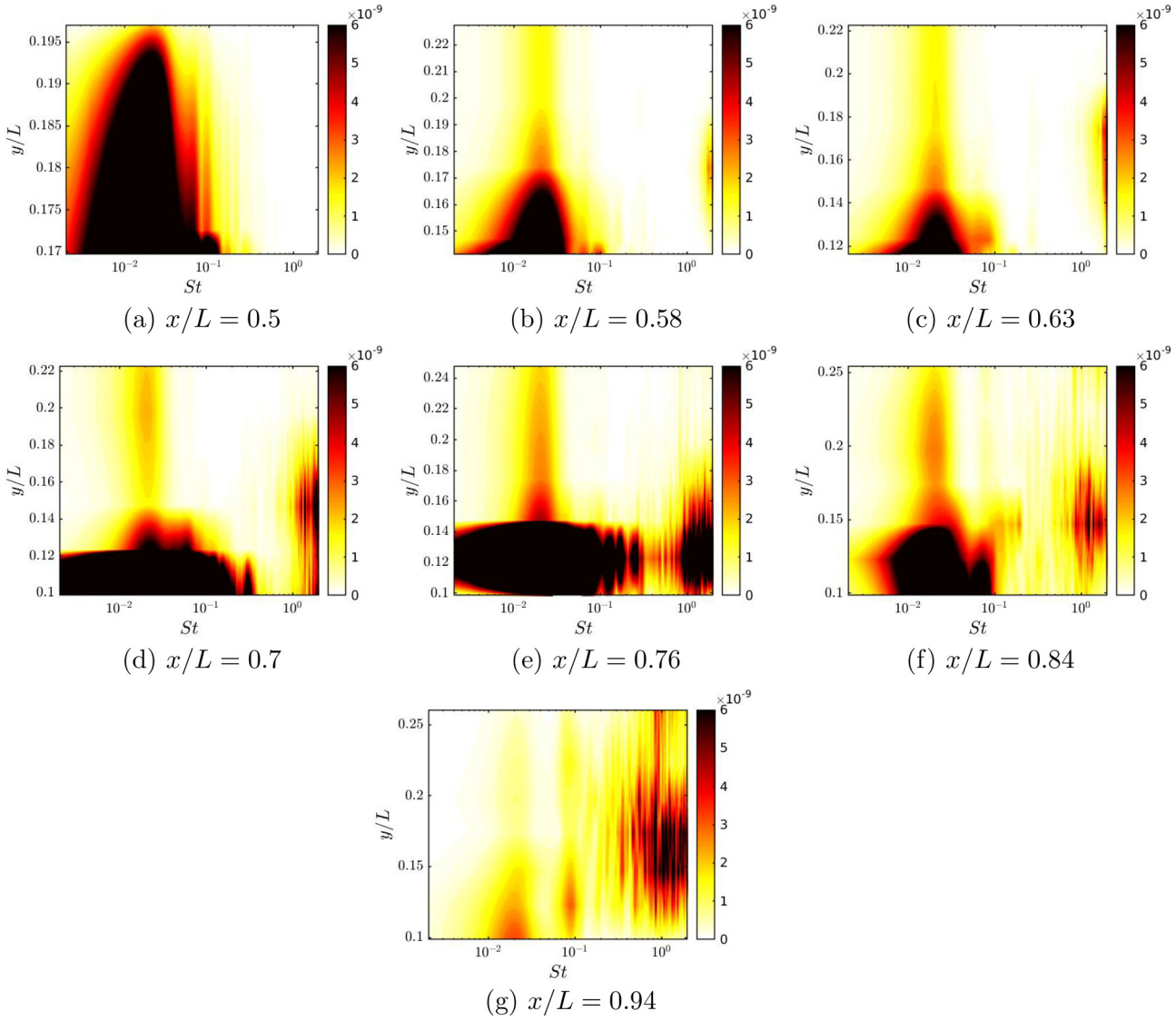

FIG. 15. Zeroth azimuthal mode pressure perturbation PSD radial distribution for different axial locations.

not more visible and the energy content seems to pass from a low-frequency broadband, prevalent related to the external shear layer, to high-frequencies contribution which characterize the fully turbulent structures near the nozzle lip.

The analysis of the second azimuthal mode distribution inside the nozzle, shown in Fig. 17, offers a scenario which is apparently very similar to the previous one, except for the fact that the emerging signature is located at $St \approx 0.3$. In fact, near the separation point the PSD spectrum exhibits for this mode a low-frequency bump and two well-visible spikes at $St \approx 0.1$ and $0.2 < St < 0.3$, but if we get away from the shear layer and we approach the wall, Fig. 13(c) shows that at this location the frequency selection at $St = 0.3$ is already present. The energy of this mode is small if compared with that at $St = 0.2$ and in contrast with the former seems to stay quite constant moving downstream toward the triple point ($x/L \approx 0.7$). Moreover, even though it is energized at the triple point as the first azimuthal component, its signature in the separated region rapidly vanishes. Moving more and more downstream, the more energetic characteristic of the shear layer as well the fully developed turbulent structures near the nozzle lip masks its presence, but if we look at the wall we can note its presence.

To conclude our analysis, a pre-multiplied PSD spectrum for the pressure perturbation p' is extracted along the nozzle axis and shown in Fig. 18. Given that the axis is a degenerated tube with a null radius, there is no possibility to separate the different azimuthal contributions. Here, all the energy is located at the average position of the Mach disks. As expected, the second Mach disk is much less energetic than the first one. However, both exhibit a lower-frequency broad band energy

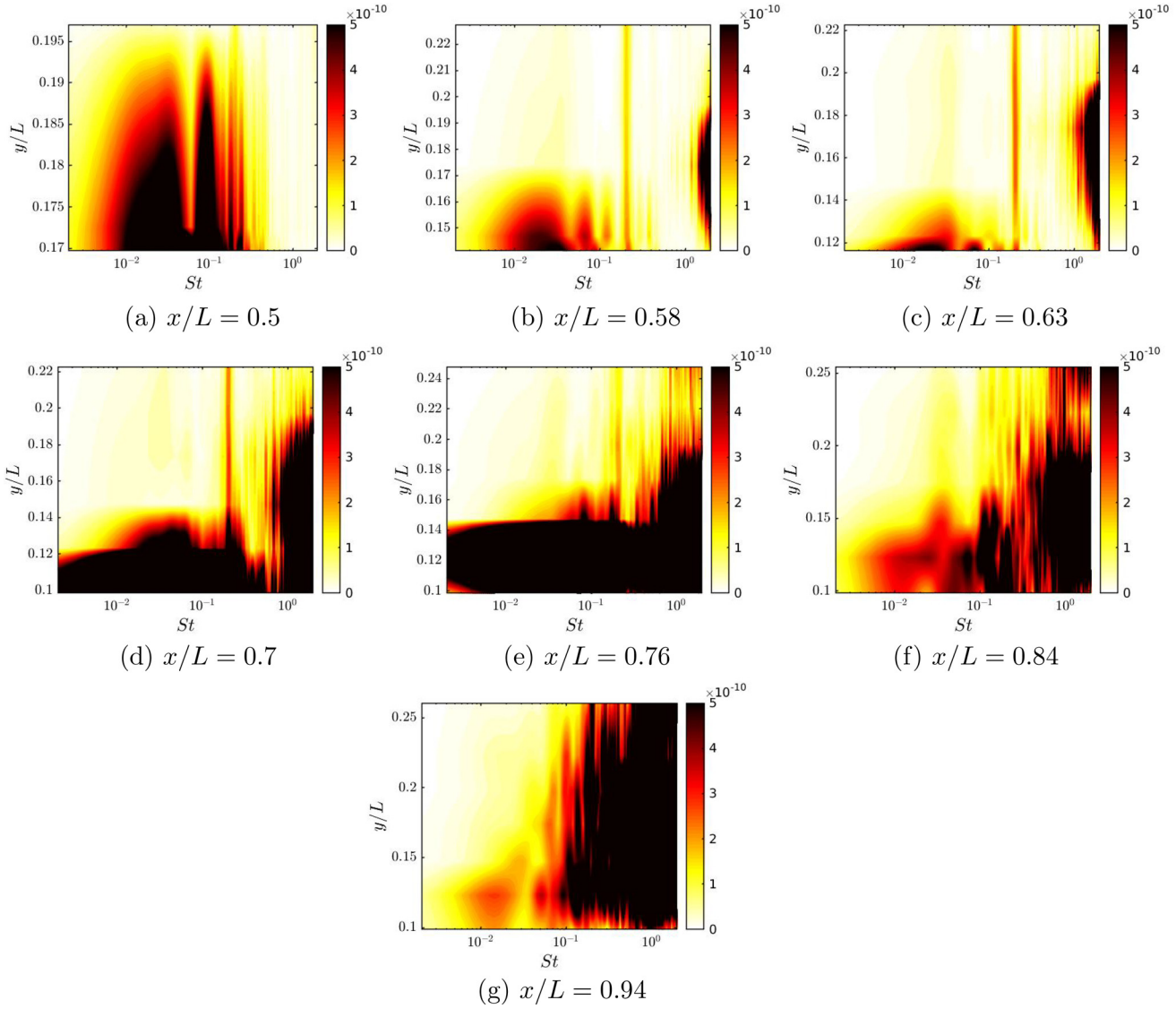

FIG. 16. First azimuthal mode pressure perturbation PSD radial distribution for different axial locations.

content, which is quite similar to that observed at the separation point. This suggests that the shock system oscillates rigidly with the separation point but the second Mach disk participates with a very low amplitude if compared with the first one.

VI. PHYSICAL ANALYSIS

We saw in Sec. V that the dynamics in the separated region, inside the supersonic nozzle considered in this work, has a specific signature in frequency. This signature is expressed by two modes with different frequencies and spatial symmetry. Particularly, the high-frequency unsteadiness is related to a $m = 2$ azimuthal mode, while the low-frequency one to a $m = 1$. In the regime at NPR = 9, the most energetic mode is the low-frequency mode at $St = 0.2$, while the high-frequency mode at $St = 0.3$ is less energetic. Conversely, preliminary DDES calculations in Tarsia Morisco[55] shown at NPR = 6 a different condition: the high-frequency mode ($St = 0.3$) is energetic as the low-frequency one ($St = 0.2$), while at NPR = 12 only the mode at $St = 0.2$ exists but it is very weak. Experiments in Jaunet *et al.*[9] confirm the DDES simulations in terms of frequency contents.[55] However, until now no clear mechanism has been proposed to explain such a phenomenon.

On the other hand, in under-expanded nozzles the reason behind the self-sustained unsteadiness is a well-known feedback close-loop mechanism known as screech. In this case, turbulent structures are conveyed in the mixing layer and interacts with the network of shock cells. Such interaction creates acoustic waves that, spreading upstream, excite the mixing layer at the outlet of the nozzle. This excitation give rises to the disturbances in the mixing layer which in turn produce

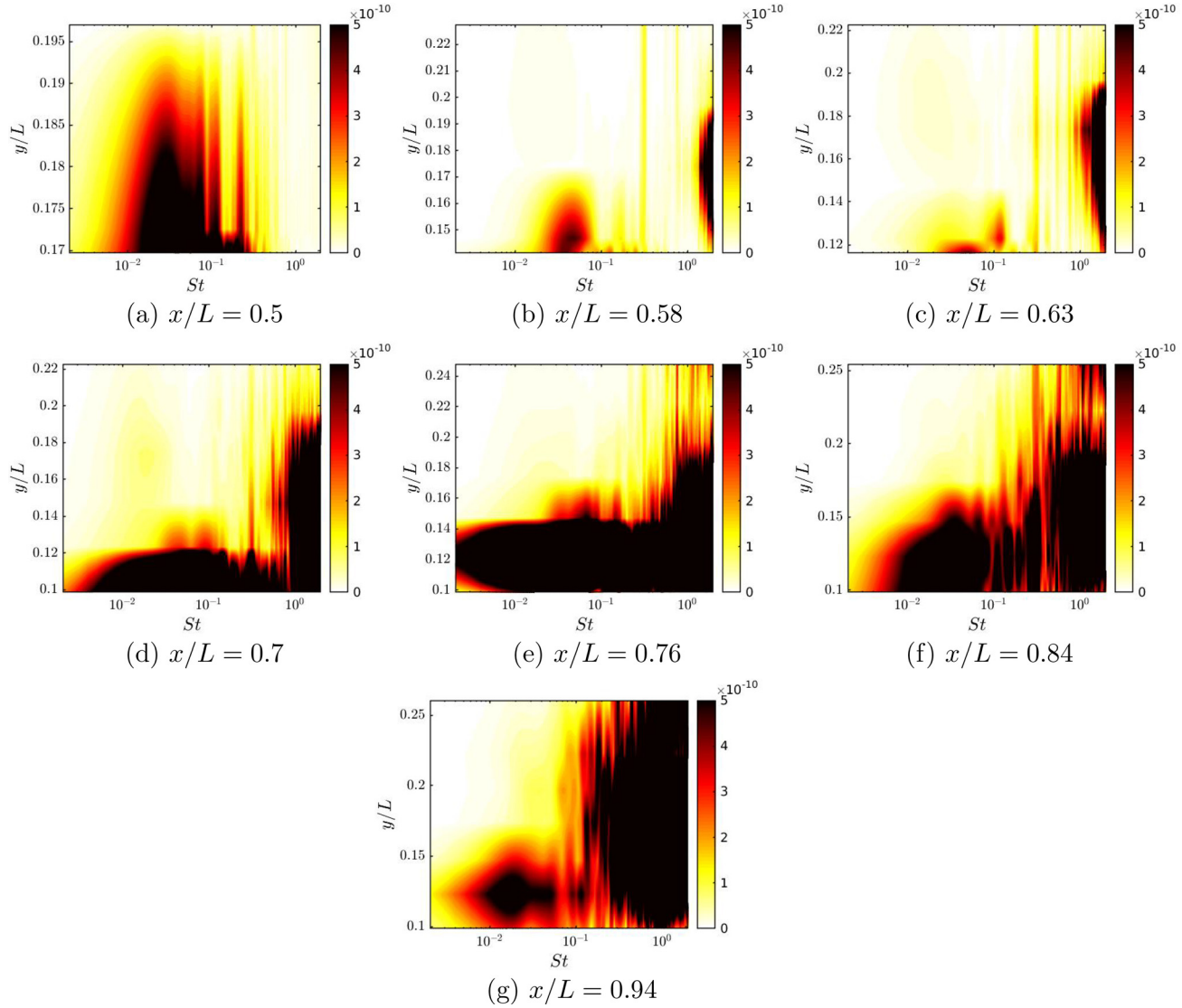

FIG. 17. Second azimuthal mode pressure perturbation PSD radial distribution for different axial locations.

turbulent structures, closing the loop. Tam *et al.*[24] realized that screech frequencies (f) collapse on the same curve inversely decreasing with the fully expanded jet Mach number (M_j), when the fully expanded exit diameter (D_j) and velocity (U_j) are used as the length and the velocity scale of the Strouhal number (St).

Until now in this work, we talked about two particular modes at $St = 0.2$ and $St = 0.3$. It is worth remembering that the length scales used to define such Strouhal numbers come from the under-expanded jets literature. In this context, the fully expanded jet velocity U_j and jet diameter D_j are the correct length scales because of the mainly acoustic nature of the phenomenon involved. This is the reason why Tam's correlation works so good to predict screech frequencies. However, clearly such length scales could not be representative for phenomena with different nature and/or different characteristic scales. An interesting consideration is that, for the nozzle here considered, only the frequency of the first azimuthal mode ($St \approx 0.2$) matches the screech correlation formula. In addition, this matching works for all the NPR (M_j) considered, as shown in Fig. 19, and was also observed in the experiments.[9] Therefore, it is very likely that the first azimuthal mode could be related to a screech-like phenomenon, involving an acoustic feedback loop. On the other hand, the $St = 0.3$ mode seems to have a different nature.

In Sec. V, a spectral analysis based on the azimuthal PSD of the pressure perturbation has shown that both modes have birth in the first external shear layer before the triple point. Both survive in the separated region, where they behave as a signature up to the wall. A qualitative analysis of the instantaneous field in terms of density gradient in Sec. III has shown in the separated region the formation of vortex

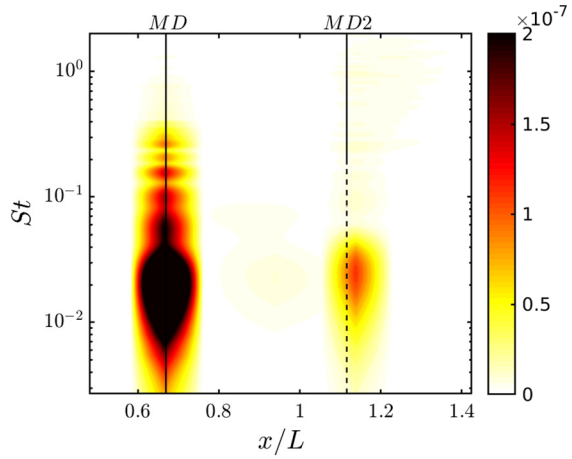

FIG. 18. Pressure perturbation PSD spectrum along the nozzle axis. MD and MD2 stand for first Mach and second Mach disk position, respectively.

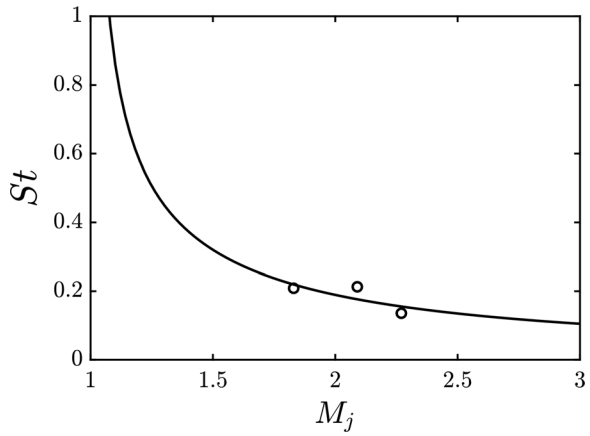

FIG. 19. Comparison between Tam's correlation[24] and first azimuthal mode spike frequency at different values of NPR (M_j). The same correlation was already observed in the experiments.[9]

shedding due to the roll-up of the supersonic shear layers. Therefore, it is very likely that both modes are related to such turbulent eddies.

This scenario involves an interaction between the Kelvin–Helmholtz instability in the supersonic shear layer, and the von-Kármán instability in the separated region, necessarily. In addition, this interaction is known to happen when a separated shear layer occurs in a cavity. In this case, shear layers become unstable and roll up in vortex-shedding vortices. The resulting instability is called impinging shear layer instability.[58] Moreover, such instability can occur with multiple vortex shedding modes at different frequencies. This happens, for example, in the vortex excitation of a prism with elongated cross section.[58] In this case, it has been shown that the same Strouhal number $\overline{St}$ can be obtained for all the modes if the correct length scales are adopted to build it. It is in the authors' opinion that the same phenomenon occurs inside the nozzle at NPR = 9: here the external supersonic shear layer rolls up in turbulent eddies producing the signatures at $St = 0.2$ and $St = 0.3$. In this case, even though both

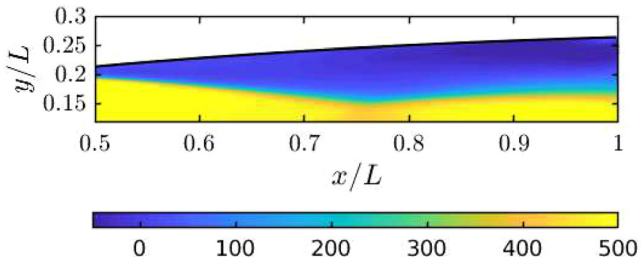

FIG. 20. Contours of the time average streamwise velocity $\overline{u}$(m/s) inside the supersonic nozzle, at NPR = 9.

modes have the same origin, i.e., the supersonic shear layer, they could be related to different velocity scales. The model proposed here suggests that the mode $m = 1$ is the expression of a perturbation propagating with the local speed of sound a, as an acoustic mode. On the other hand, the nature of the $m = 2$ mode could be hydrodynamic. In this perspective, the latter would be the result of a perturbation conveyed with a convection velocity u, which would be the streamwise velocity of the supersonic shear layer. To have a feedback close loop, both modes require the same characteristic distance d, i.e., the traveled distance inside the loop. Thus, the following relation for the impinging shear layer instability must be fulfilled:

$$\overline{St} = \frac{f_{St=0.2} \cdot d}{a} = \frac{f_{St=0.3} \cdot d}{u}, \tag{13}$$

where $f_{St=0.2}$ (respectively, $f_{St=0.3}$) is the dimensional frequency of the mode at $St = 0.2$ (respectively, $St = 0.3$).

To verify the plausibility of the model proposed, let us have a look at Figs. 20 and 21, which show the average streamwise velocity $\overline{u}$ and the local speed of sound $\overline{a}$ field, respectively. In the separated region, the time average local speed of sound is $\overline{a} \approx 320$ m/s, while in the external supersonic shear layer, the time average streamwise velocity is $\overline{u} \approx 485$ m/s.

Therefore, if we replace a (respectively, u) with $\overline{a}$ (respectively, $\overline{u}$) in Eq. (13),

$$\frac{St_1}{St_2} = \frac{f_{St=0.2}}{f_{St=0.3}} = \frac{\overline{a}}{\overline{u}} \approx 0.66, \tag{14}$$

which supports the scenario proposed. This means that both modes are compatible with a vortex shedding related to the impinging shear layer instability of the supersonic shear layer. The dimensional analysis would suggest that the $m = 1$ mode at $St = 0.2$ could be related to an acoustic radiation (as confirmed by Tam's correlation), while the $m = 2$

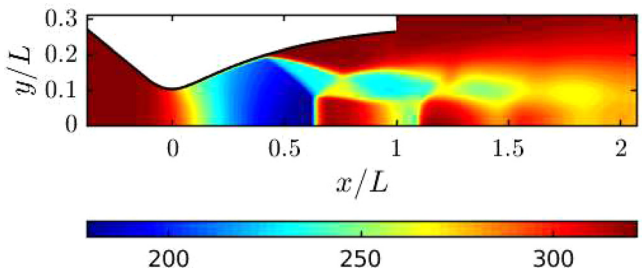

FIG. 21. Contours of the time average local speed of sound $\overline{a}$ (m/s) at NPR = 9.

one at $St = 0.3$ to a hydrodynamic product. For this reason, it is very likely that the turbulent eddies detaching from the external shear layer are such hydrodynamic product. Here, due to the supersonic nature of the shear layer, the acoustic mode has a lower frequency than the hydrodynamic one. Finally, the contribution at $St \approx 0.02$ seems to be related to the shock displacement about the separation point.

From Table III, we know that the time average separation point is $x_s \approx 0.4\ L$, and consequently the traveled distance is $d \approx 0.6\ L$. With this new length scales, the modified Strouhal numbers for both modes would be

$$\overline{St}_1 = \frac{f_1 \cdot 0.6\ L}{\overline{a}} \approx 0.65, \quad \overline{St}_2 = \frac{f_2 \cdot 0.6\ L}{\overline{u}} \approx 0.64, \tag{15}$$

which are in practice the same and support the model proposed. This result is quite surprising because a Strouhal number $\overline{St} = f \cdot d/U_c \approx 0.6$ is commonly observed in previous experiments involving impinging shear layer instabilities.[58,59]

At this point, we need to find the large-scale flow which maintains the feedback loop. To do that, let us consider the time average Mach number field $\overline{M}$ in Fig. 22. In this figure, streamlines, which are denoted with continuous black lines, indicate the presence of a recirculation region well visible at the nozzle lip. The same flow features were already observed by Martelli *et al.*[22] in an over-expanded TIC experiencing an FSS regime.

The mechanism proposed here is based on an acoustic–hydrodynamic feedback loop involving the shear layer instability and the separation bubble at the nozzle lip. There are many cases in the literature, in which the separation bubble acts as an amplifier of acoustic

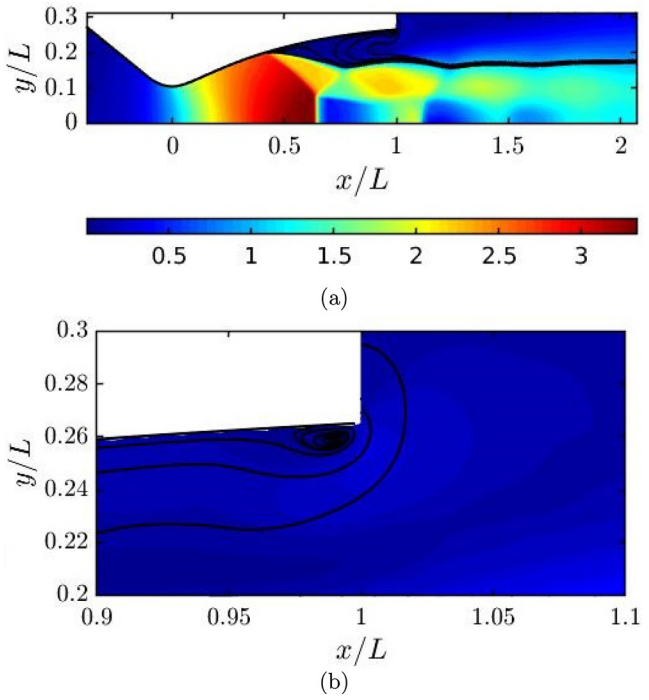

FIG. 22. Contours of the mean Mach number $\overline{M}$ at NPR = 9. Streamlines are denoted with a solid black line. (b) is a zoom of the recirculation region near the nozzle lip.

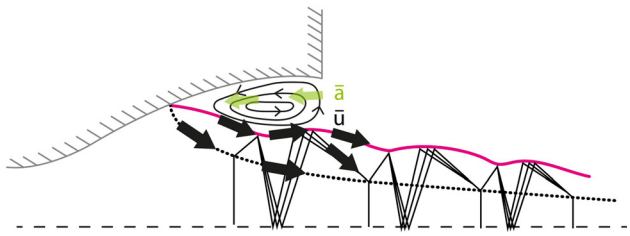

FIG. 23. Sketch of the mechanism linked to the high-frequency modes. The hydrodynamic mode at $St = 0.3$ is related to a perturbation conveyed with a velocity $\overline{u}$ in the external supersonic shear layer. The screech-like mode is related to the perturbation radiating at the speed of sound $\overline{a}$. Both modes are the expression of a Kelvin–Helmholtz instability at $\overline{St} \approx 0.65$. The large-scale flow maintaining the feedback loop is the recirculation bubble at the nozzle lip.

disturbances.[60,61] For instance, the transitional airfoil experiences acoustic feedback-loop mechanisms involving multiple tones.[62–64] In these cases, hydrodynamic perturbations originate at the leading edge and conveyed downstream. The disturbances are amplified by the recirculation bubble on the airfoil surface, and, at the trailing edge, acoustic waves radiate upstream triggering new disturbances. For the case examined in this work, we propose a similar mechanism. In this regard, let us rely on the sketch in Fig. 23. Some pressure fluctuations radiate from the separation bubble up to the separation point in the time $t_1 = d/a$, where d is the distance traveled and a is the local speed of sound in the separated region. These fluctuations generate some kind of disturbances at the separation point that are conveyed in the mixing layer downstream with a convection speed u in the time $t_2 = d/u$, with u the average velocity inside the external supersonic shear layer. Later, such disturbances interact with the recirculating bubble for a period of time $t_3 = 1/f_b$, where f_b is the frequency of the bubble. According to this scenario, the following relation must be fulfilled:

$$\frac{d}{\overline{u}} + N\frac{1}{f_b} = \frac{d}{\overline{a}}, \tag{16}$$

where the traveled distance d is the distance between the nozzle lip and the separation point, while f_b is the frequency of the separation bubble. With $N = 1$, Eq. (16) reduces to

$$\frac{1}{f_b} = d\left(\frac{1}{\overline{a}} - \frac{1}{\overline{u}}\right),$$

which, with relation (14) becomes

$$f_b\ 0.6\ L = \frac{St_2\ a}{St_2 - St_1}.$$

After injecting Eqs. (11) and (12) in the above relation, a frequency $St_b \approx 0.9$ is obtained. The reader can easily note that such frequency is compatible with the high-frequency bump ($St \approx 1$) well visible near the nozzle lip in the wall pressure PSD spectra in Fig. 13.

VII. CONCLUSION AND PERSPECTIVES

This paper brings several insights in the understanding of the unsteady dynamics which characterizes over-expanded TIC nozzles operating in a free shock separation regime. Previous experimental data recorded two high-frequency signatures with specific azimuthal symmetry (m = 1 and m = 2) at different axial locations on the walls

of the nozzle. To reproduce this condition, the dynamics of the same TIC nozzle at a fixed pressure ratio NPR = 9 has been modeled by means of a delayed detached eddy simulation (DDES). Such dynamics involves shock-boundary layer interaction, supersonic shear layers, vortex shedding, and recirculation bubbles.

In order to understand the mechanism behind the characteristic high-frequency signatures, a pressure perturbation power spectral density (PSD) has been performed on different axial rings inside the nozzle. The richness of the resulting spectral content required a long time signal to have reasonably converged statistics to be compared with the experimental data. The resulting spectra return two spikes with the expected specific selection in frequency and spatial domain. These modes have birth in the external shear layer and persist in the separated region up to the wall. This suggests that the formation of these two modes could be strictly related to the supersonic shear layer. The analysis of the instantaneous field leads the authors to link both the modes to the vortex shedding produced by a particular shear layer instability. The hypothesis is supported by the fact that if we relate the low-frequency mode to the local speed of sound in the separated region and the high-frequency mode to the velocity in the supersonic shear layer, the same modified Strouhal number is obtained. Moreover, numerical results and experimental findings have observed only the m = 1 mode collapsing on Tam's correlation formula for the screech, supporting an acoustic-like behavior for this mode. In this scenario, the authors propose an acoustic–hydrodynamic feedback loop maintained by a recirculation bubble at the nozzle lip, which produces acoustic waves. These waves excite the separation point, which triggers in turn the supersonic shear layer roll-up and the consequent vortex shedding.

Regarding the perspectives of this work, the authors are planning to push forward the analysis of the dynamics related to these two high-frequency modes. As shown in this work, URANS calculations were not capable of describing the above-mentioned dynamics. However, it could be possible that these modes are linearly stable and need nonlinear fluctuations to be triggered. In this scenario, a linear stability analysis performed about the fixed point of the URANS equations (i.e., the RANS solution) would answer this question.

ACKNOWLEDGMENTS

This work was accomplished in the frame of ATAC (Aérodynamique des Tuyères et des Arrières Corps) Group led by CNES. The experimental tests were performed at Pprime Institute. The authors would like to thank Steve Girard and Vincent Jaunet for sharing the experimental data used in this work. The authors gratefully acknowledge ArianeGroup for the support. The computations were performed thanks to the HPC resources from GENCI-[CCRT/CINES/IDRIS] (Grant Nos. A0052A06362 and A0072A06362).

AUTHOR DECLARATIONS

Conflict of Interest

The authors have no conflicts to disclose.

Author Contributions

Cosimo Tarsia Morisco: Conceptualization (equal); Validation (equal); Visualization (equal); Writing – original draft (equal); Writing – review & editing (equal). **Jean-Christophe Robinet:** Conceptualization (equal); Validation (equal); Visualization (equal); Writing – original draft (equal); Writing – review & editing (equal). **Julien Herpe:** Writing – review & editing (equal). **Didier Saucerau:** Writing – review & editing (equal).

DATA AVAILABILITY

The data that support the findings of this study are available from the corresponding author. Restrictions apply to the availability of these data, which were used under license for this study. Data are available from the authors upon reasonable request and with the permission of CNES.

REFERENCES

[1]L. Nave and G. Coffey, "Sea level side loads in high-area-ratio rocket engines," in 9th Propulsion Conference, 1973.
[2]M. Sajben, J. Kroutil, and C. Chen, "A high-speed schlieren investigation of diffuser flows with dynamic distortion," in *13th Propulsion Conference* (AIAA, 1977), p. 875.
[3]T. Bogar, M. Sajben, and J. Kroutil, "Characteristic frequencies of transonic diffuser flow oscillations," AIAA J. **21**, 1232–1240 (1983).
[4]M. Sajben and J. Kroutil, "Effects of initial boundary-layer thickness on transonic diffuser flows," AIAA J. **19**, 1386–1393 (1981).
[5]T. Bogar, "Structure of self-excited oscillations in transonic diffuser flows," AIAA J. **24**, 54–61 (1986).
[6]L. Torngren, "Correlation between outer flow and internal nozzle pressure fluctuations," in *Fourth Symposium on Aerothermodynamics for Space Vehicles* (European Space Agency, 2002), Vol. 487, p. 415.
[7]J. Östlund, T. Damgaard, and M. Frey, "Side-load phenomena in highly overexpanded rocket nozzles," J. Propul. Power **20**, 695–704 (2004).
[8]W. J. Baars, C. E. Tinney, J. H. Ruf, A. M. Brown, and D. M. McDaniels, "Wall pressure unsteadiness and side loads in overexpanded rocket nozzles," AIAA J. **50**, 61–73 (2012).
[9]V. Jaunet, S. Arbos, G. Lehnasch, and S. Girard, "Wall pressure and external velocity field relation in overexpanded supersonic jets," AIAA J. **55**, 4245–4257 (2017).
[10]C.-L. Chen, S. Chakravarthy, and C. Hung, "Numerical investigation of separated nozzle flows," AIAA J. **32**, 1836–1843 (1994).
[11]V. Brunet, "Computational study of buffet phenomenon with unsteady RANS equations," AIAA Paper No. 2003-3679, 2003.
[12]S. Deck, "Numerical simulation of transonic buffet over a supercritical airfoil," AIAA J. **43**, 1556–1566 (2005).
[13]M. Thiery and E. Coustols, "Numerical prediction of shock induced oscillations over a 2D airfoil: Influence of turbulence modelling and test section walls," Int. J. Heat Fluid Flow **27**, 661–670 (2006).
[14]S. Deck and P. Guillen, "Numerical simulation of side loads in an ideal truncated nozzle," J. Propul. Power **18**, 261–269 (2002).
[15]S. Deck and A. T. Nguyen, "Unsteady side loads in a thrust-optimized contour nozzle at hysteresis regime," AIAA J. **42**, 1878–1888 (2004).
[16]J. Moríñigo and J. Salvá, "Three-dimensional simulation of the self-oscillating flow and side-loads in an over-expanded subscale rocket nozzle," Proc. Inst. Mech. Eng., Part G **220**, 507–523 (2006).
[17]B. J. Olson and S. K. Lele, "A mechanism for unsteady separation in over-expanded nozzle flow," Phys. Fluids **25**, 110809 (2013).
[18]B. Zebiri, A. Piquet, A. Hadjadj, and S. Verma, "Shock-induced flow separation in an overexpanded supersonic planar nozzle," AIAA J. **58**, 2122–2131 (2020).
[19]P. Spalart, W.-H. Jou, M. Strelets, and S. Allmaras, "Comments on the feasibility of les for wings, and on a hybrid RANS/LES approach," in Proceedings of First AFOSR International Conference on DNS/LES, 1997.
[20]S. Deck, "Delayed detached eddy simulation of the end-effect regime and side-loads in an overexpanded nozzle flow," Shock Waves **19**, 239–249 (2009).
[21]A. Shams, G. Lehnasch, P. Comte, H. Deniau, and T. A. de Roquefort, "Unsteadiness in shock-induced separated flow with subsequent reattachment of supersonic annular jet," Comput. Fluids **78**, 63–74 (2013).

[22]E. Martelli, L. Saccoccio, P. Ciottoli, C. Tinney, W. Baars, and M. Bernardini, "Flow dynamics and wall-pressure signatures in a high-Reynolds-number over-expanded nozzle with free shock separation," J. Fluid Mech. **895**, A29 (2020).
[23]F. Bakulu, G. Lehnasch, V. Jaunet, E. Goncalves, and S. Girard, "Jet resonance in truncated ideally contoured nozzles," J. Fluid Mech. **919**, A32 (2021).
[24]C. K. Tam, J. M. Seiner, and J. Yu, "Proposed relationship between broadband shock associated noise and screech tones," J. Sound Vib. **110**, 309–321 (1986).
[25]T. Hsieh, T. Bogar, and T. Coakley, "Numerical simulation and comparison with experiment for self-excited oscillations in a diffuser flow," AIAA J. **25**, 936–943 (1987).
[26]K. Zaman, M. Dahl, T. Bencic, and C. Loh, "Investigation of a transonic resonance with convergent-divergent nozzles," J. Fluid Mech. **463**, 313 (2002).
[27]H. Y. Wong, "Theoretical prediction of resonance in nozzle flows," J. Propul. Power **21**, 300–313 (2005).
[28]A. Powell, "On the noise emanating from a two-dimensional jet above the critical pressure," Aeronaut. Q. **4**, 103–122 (1953).
[29]G. Raman, "Advances in understanding supersonic jet screech: Review and perspective," Prog. Aerosp. Sci. **34**, 45–106 (1998).
[30]S. Verma, M. Chidambaranathan, and A. Hadjadj, "Analysis of shock unsteadiness in a supersonic over-expanded planar nozzle," Eur. J. Mech.-B **68**, 55–65 (2018).
[31]E. Martelli, P. Ciottoli, L. Saccoccio, F. Nasuti, M. Valorani, and M. Bernardini, "Characterization of unsteadiness in an overexpanded planar nozzle," AIAA J. **57**, 239–251 (2019).
[32]D. Edgington-Mitchell, V. Jaunet, P. Jordan, A. Towne, J. Soria, and D. Honnery, "Upstream-travelling acoustic jet modes as a closure mechanism for screech," J. Fluid Mech. **855**, R1 (2018).
[33]J. L. Weightman, O. Amili, D. Honnery, D. Edgington-Mitchell, and J. Soria, "Nozzle external geometry as a boundary condition for the azimuthal mode selection in an impinging underexpanded jet," J. Fluid Mech. **862**, 421–448 (2019).
[34]P. R. Spalart, S. Deck, M. L. Shur, K. D. Squires, M. K. Strelets, and A. Travin, "A new version of detached-eddy simulation, resistant to ambiguous grid densities," Theor. Comput. Fluid Dyn. **20**, 181 (2006).
[35]P. Spalart and S. Allmaras, "A one-equation turbulence model for aerodynamic flows," in *30th Aerospace Sciences Meeting and Exhibit* (AIAA, 1992), p. 439.
[36]B. Aupoix and P. R. Spalart, "Extensions of the Spalart–Allmaras turbulence model to account for wall roughness," Int. J. Heat Fluid Flow **24**, 454–462 (2003).
[37]S. Allmaras, F. Johnson, and P. Spalart, "Modifications and clarifications for the implementation of the Spalart-Allmaras turbulence model," in Seventh International Conference on Computational Fluid Dynamics (ICCFD7), 2012.
[38]J. R. Edwards and S. Chandra, "Comparison of eddy viscosity-transport turbulence models for three-dimensional, shock-separated flowfields," AIAA J. **34**, 756–763 (1996).
[39]C. Mockett, "A comprehensive study of detached-eddy simulation," Ph.D. thesis (Technische Universitat, Berlin, 2009).
[40]S. Deck, "Recent improvements in the zonal detached eddy simulation (ZDES) formulation," Theor. Comput. Fluid Dyn. **26**, 523–550 (2012).
[41]N. Chauvet, S. Deck, and L. Jacquin, "Zonal detached eddy simulation of a controlled propulsive jet," AIAA J. **45**, 2458–2473 (2007).
[42]J. Riou, E. Garnier, S. Deck, and C. Basdevant, "Improvement of delayed-detached eddy simulation applied to separated flow over missile fin," AIAA J. **47**, 345–360 (2009).
[43]G. Pont, "Self adaptive turbulence models for unsteady compressible flows modèles de turbulence auto-adaptatifs pour la simulation des écoulements compressibles instationnaires," Ph.D. thesis (Ecole Nationale Supérieure D'arts et métiers - ENSAM, 2015).
[44]E. Goncalves and R. Houdeville, "Numerical simulations of a transport-aircraft configuration," Int. J. Comput. Fluid Dyn. **23**, 449–459 (2009).
[45]A. Jameson, W. Schmidt, and E. Turkel, "Numerical solution of the Euler equations by finite volume methods using Runge Kutta time stepping schemes," in 14th Fluid and Plasma Dynamics Conference, 1981.
[46]S. R. Chakravarthy, "Development of upwind schemes for the Euler equations," NASA Report No. 4043, 1987.
[47]S. H. Park and J. H. Kwon, "Implementation of $\kappa - \omega$ turbulence models in an implicit multigrid method," AIAA J. **42**, 1348–1357 (2004).
[48]F. Liu and X. Zheng, "A strongly coupled time-marching method for solving the Navier-Stokes and κ-ω turbulence model equations with multigrid," J. Comput. Phys. **128**, 289–300 (1996).
[49]H. Luo, J. D. Baum, and R. Löhner, "A fast, matrix-free implicit method for compressible flows on unstructured grids," J. Comput. Phys. **146**, 664–690 (1998).
[50]H. Luo, J. D. Baum, and R. Löhner, "An accurate, fast, matrix-free implicit method for computing unsteady flows on unstructured grids," Comput. Fluids **30**, 137–159 (2001).
[51]J. Delery, *Aérodynamique Interne, Tuyères et Arrières Corps* (ENSAE, 1989).
[52]G. B. Whitham, *Linear and Nonlinear Waves* (John Wiley & Sons, 2011), Vol. 42.
[53]J. Blazek, *Computational Fluid Dynamics: Principles and Applications* (Butterworth-Heinemann, 2015).
[54]D. Whitfield, "Three-dimensional unsteady Euler equations solution using flux vector splitting," in 17th Fluid Dynamics, Plasma Dynamics, and Lasers Conference, 1984.
[55]C. Tarsia Morisco, "Nonlinear dynamics and linear stability analysis of over-expanded nozzle flows," Ph.D. thesis (HESAM Université, 2020).
[56]A. Kistler, "Fluctuating wall pressure under a separated supersonic flow," J. Acoust. Soc. Am. **36**, 543–550 (1964).
[57]M. Otis and J. Solomon, "PSD computations using Weltch method," Report No. SAND-91-1533 (Sandia National Laboratories, New Mexico, 1991).
[58]Y. Nakamura and M. Nakashima, "Vortex excitation of prisms with elongated rectangular, h and ⊢ cross-sections," J. Fluid Mech. **163**, 149–169 (1986).
[59]D. Rockwell and E. Naudascher, "Self-sustaining oscillations of flow past cavities," J. Fluids Eng. **100**, 152 (1978).
[60]O. Marquet, D. Sipp, J.-M. Chomaz, and L. Jacquin, "Amplifier and resonator dynamics of a low-Reynolds-number recirculation bubble in a global framework," J. Fluid Mech. **605**, 429–443 (2008).
[61]D. Rodríguez, E. M. Gennaro, and M. P. Juniper, "The two classes of primary modal instability in laminar separation bubbles," J. Fluid Mech. **734**, R4 (2013).
[62]G. Desquesnes, M. Terracol, and P. Sagaut, "Numerical investigation of the tone noise mechanism over laminar airfoils," J. Fluid Mech. **591**, 155–182 (2007).
[63]M. F. De Pando, P. J. Schmid, and D. Sipp, "A global analysis of tonal noise in flows around aerofoils," J. Fluid Mech. **754**, 5–38 (2014).
[64]T. R. Ricciardi, W. R. Wolf, and K. Taira, "Transition, intermittency and phase interference effects in airfoil secondary tones and acoustic feedback loop," J. Fluid Mech. **937**, A23 (2022).